# Deep-sea Robotic Survey and Data Processing Methods for Regional Scale Estimation of Manganese Crust Distribution

Umesh Neettiyath, Blair Thornton, Mehul Sangekar, Yuya Nishida, Kazuo Ishii, Adrian Bodenmann, Takumi Sato, Tamaki Ura, and Akira Asada

**Abstract**

Manganese crusts (Mn-crusts) are a type of mineral deposit that exists on the surface of seamounts and guyots at depths of $> 800m$. We have developed a method to efficiently map their distribution using data collected by autonomous underwater vehicles and remotely operated vehicles. Volumetric measurements of Mn-crusts are made using a high-frequency sub-surface sonar and a 3D visual mapping instrument mounted on these vehicles. We developed an algorithm to estimate Mn-crust distribution by combining continuous sub-surface thickness measurements with exposed surface area identified in 3D maps. This is applied to data collected from three expeditions at Takuyo Daigo seamount at depths of $\sim 1400\,m$. The transects add to $\sim 11\,km$ in length with $12,510\,m^2$ mapped. The results show that 52 % of the surveyed area is covered by Mn-crusts with a mean thickness of 70 mm. The mean Mn-crust occurrence is $69.6\,kg/m^2$ with a maximum of $204\,kg/m^2$ in the mapped region. The results are consistent with estimates made from samples retrieved from the area, showing more detailed

U. Neettiyath, M. Sangekar and A. Asada are with the Institute of Industrial Science, The University of Tokyo, Japan (e-mail: umesh@iis.u-tokyo.ac.jp)

B. Thornton is an Associate Professor in the Centre for In situ and Remote Intelligent Sensing, Faculty of Engineering and Physical Science, The University of Southampton, with an adjunct position at the Institute of Industrial Science, The University of Tokyo, Japan

Y. Nishida is with the Frontier Research Academy for Young Researchers, Kyushu Institute of Technology, Kitakyushu, Japan

K. Ishii is a Professor at the Department of Human Intelligence Systems, Kyushu Institute of Technology, Kitakyushu, Japan

A. Bodenmann is a senior research assistant at the Maritime Robotics Laboratory, Southampton Marine and Maritime Institute, University of Southampton, Southampton, UK

T. Sato is with the Offshore Advanced Technology Department at the National Maritime Research Institute, Tokyo, Japan

T. Ura is with the Center for Socio-Robotic Synthesis, Kyushu Institute of Technology, Kitakyushu, Japan

distribution patterns and having significantly lower uncertainty bounds for regional scale Mn-crust inventory estimation.

**Index Terms**

Unmanned underwater vehicles, Manganese Crust, Sub-bottom acoustics, Deep sea survey, Visual reconstruction, Mineral exploration, Aquatic robots.

## I. Introduction

Cobalt-rich Manganese crusts (Mn-crust) form on the slopes and shoulders of seamounts and guyots in geologically stable regions. The Mn-crust layer grows over millions of years by precipitation from the ambient seawater [1], [2]. The northwestern Pacific Ocean is known to have large Mn-crust deposits spread over several hundreds of square kilometers [3]–[5]. Mn-crusts vary from 10 mm to 250 mm in thickness and are found between a depths of more than 800 m, with reports of Mn-crusts as deep as 5700 m. These deposits contain Cobalt, Nickel, Platinum and various rare earth elements, making them a potential target for mining [6]–[9]. However, the thickness of Mn-crust varies due to slope, seawater conditions, depth, historical landslides and sediment cover [2]. This makes reliable estimation of quantitative Mn-crust distribution difficult.

The survey requirements of Mn-crusts are different to Manganese nodules (Mn-nodules), found in basins between 3500 m and 6000 m depth [7], [10]–[12], where non-contact methods such as shipboard multibeam [13], [14], photogrammetry and sidescan surveys [15]–[17] from Autonomous Underwater Vehicle (AUV) and Remotely Operated Vehicle (ROV) have been applied. Mn-nodule distribution can be accurately estimated from such datasets since their distribution can be determined from surface appearance and shape alone. Accurate estimates of Mn-crust distribution requires both the subsurface thickness of the crust layer and their lateral % coverage to be known. Dredging surveys are often used to survey the thickness of Mn-crusts, but samples recovered using this method are often damaged and the method is biased towards loose rocks and edges that are more likely to be snagged. Core drilling and sampling from ROVs is effective to collect information about the thickness and elemental composition of samples whose context is understood from camera footage [2], [3], [18]. However, obtaining samples is time consuming, and the spatial resolutions achieved is limited to just a few samples every km [2]. The lateral distribution of exposed crusts can be surveyed using video or still cameras mounted on towed sleds or ROVs, where the footage is manually labelled by human

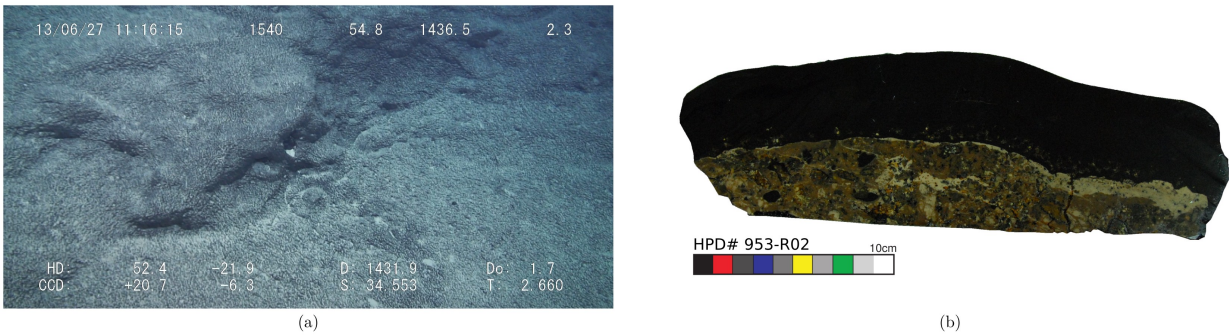


(a) (b)

Fig. 1. Mn-crusts at Takuyo Daigo seamount in the northwestern Pacific ocean. (a) Continuous Mn-crust deposits as seen from the video feed of ROV Hyper-Dolphin. (b) Cross-section of a Mn-crust sample, showing crust (black colour) deposited as a layer over a substrate rock (brown with intrusions).

experts into categories such as Mn-crusts, nodules or sediment deposits, which are compiled into estimates of distribution [4], [6]. However, manual labelling is time consuming, making it difficult to scale the operations to larger regions.

High resolution, scalable estimation of Mn-crust requires automated methods to determine the lateral distribution and thickness of Mn-crusts without physical sampling. Acoustic methods can be used to measure Mn-crust thickness as long as the Mn-crusts and their substrates have different acoustic impedances [19]. However, it can be difficult to determine if acoustic signals are of Mn-crust from their acoustic signature alone.For this, visual methods can be effective if reliable automatic classification methods can be developed [20]–[25].

This paper presents a scalable way to determine the continuous mass distribution of Mn-crust over hectare-order regions of the seafloor using visual and acoustic sensors. This builds on the work described in [19], describing modifications to the data acquisition hardware, and presenting novel data processing methods that scale to the hectare-order regions now surveyed using this system. This overcomes previous limitations, where in [19], the seafloor was segmented into regions of crust, sediment and a mix of the two using Gaussian Mixture Models (GMM) and acoustic measurements within each segment were used to estimate the abundance of crust in each region. The high computational cost of segmentation does not readily scale to larger regions. While previous work analysed small volumes of ROV data, the majority of data in this work has been collected using an AUV, described in [26], with modifications made to the data acquisition system. This includes real-time control of a double-gimbal system that orients the acoustic probe to be normal to the seafloor by analysing the 3D visual mapping data [27]. This allows acoustic

TABLE I

SPECIFICATIONS OF THE PLATFORM (AUV BOSS-A)

| Vehicle | |
|---|---|
| Dimensions | 3.0 m x 0.7 m x 0.7 m |
| Mass | 600 kg |
| Operating velocity | 0.2 kn (0.1 m/s) |
| Operating altitude range | $1.5 \pm 0.5\,m$ |
| Depth rating | 3000 m |
| Endurance | 7 h |
| Payloads | |
| **Parametric acoustic probe:** | |
| Frequency | 2 MHz (carrier) , 200 kHz (signal) |
| -3 dB footprint | $< 2\,cm$ (dynamic focusing) |
| Mounting | 2-axis gimbal |
| Gimbal roll, pitch range | $\pm 15^{\circ}$, $\pm 45^{\circ}$ |
| Ping rate | 20 Hz |
| **3D visual mapping system:** | |
| Type | Monocular vision and structured light using sheet laser |
| Illumination | 2 x LED panels (20,000 lm/panel) |
| Laser power , wavelength | 120mW , 532 nm |
| Camera resolution, FOV | 1328 x 1048, $65^{\circ}$ x $53^{\circ}$ |
| Camera frame rate | 15 fps |
| Laser to camera baseline | 1.22 m |
| Swath, resolution | 1.5 m , 1.4 mm |
| Bathymetry resolution (at 1.5 m) | 1.4 mm (cross-transect) |
| | 6.7 mm (along-transect) |
| | 3.0 mm (depth) |

measurements to be made on steep slopes and complex terrains. The advances in the sensor, platform and novel algorithms described in this paper allow estimates of Mn-crusts to be made over hectare-scale regions of the seafloor for the first time.

## II. SYSTEM OVERVIEW

### A. AUV Boss-A

The specifications of the AUV "Boss-A" [26], used to collect the data analysed in this paper, are shown in Table I and the position of various sensors are shown in Fig. 2.

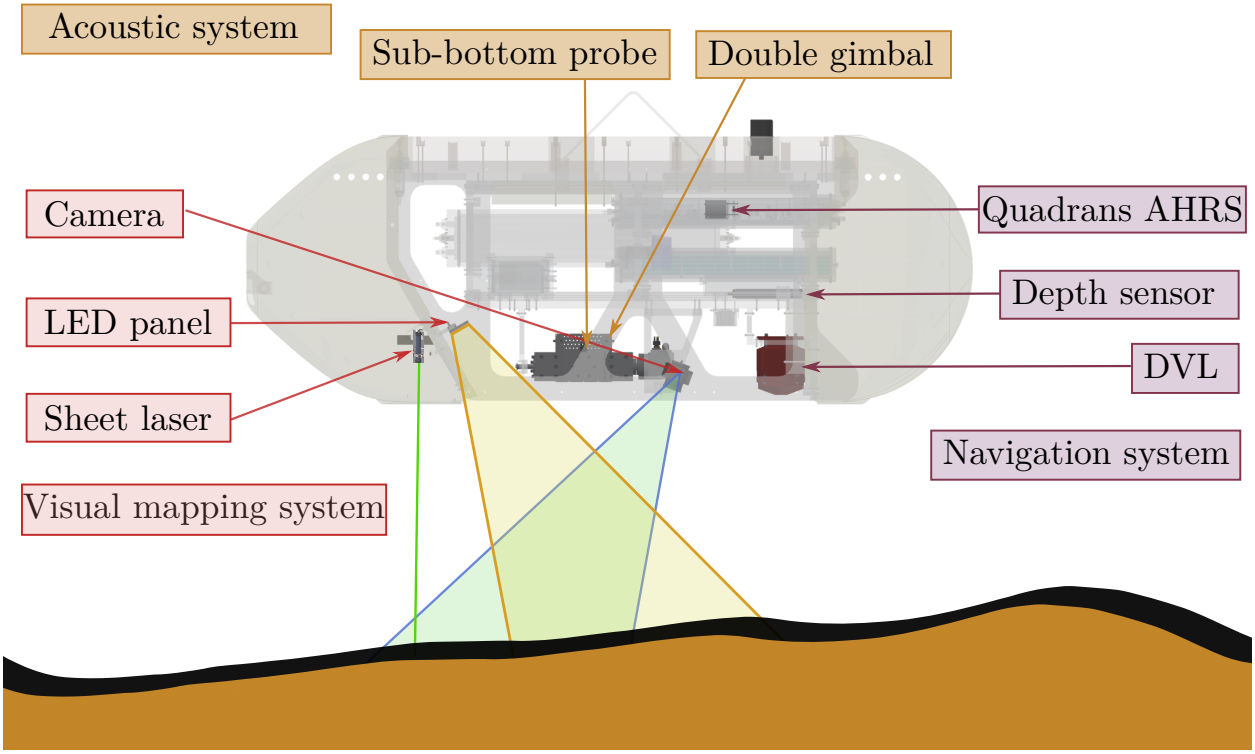


Fig. 2. Schematic representation of Boss-A surveying Mn-crust using visual and acoustic sub-systems.

The acoustic probe is a parametric sub-surface sonar that records sub-surface reflections of the seafloor. The probe consists of a 5 channel annular array of 2 MHz piezoelectric transducers for transmission and a 200 kHz piezoelectric transducer to record reflections. It is dynamically focused on the seafloor at ranges from 0.5 m to 2.5 m [19]. Since measurements require the probe to be orthogonal to the measured surface for best results, the probe is mounted on a two axis gimbal. The relative slope of the seafloor is calculated in real-time and the gimbals oriented normal to the seafloor [27]. The signals are analysed to find reflections from the crust-substrate boundary and thickness values are calculated as described in section III-B.

The visual system generates 3D colour maps of the seafloor using a light sectioning method using a single camera, a sheet laser and LEDs for illumination as described in [28]. The deformation of the laser line, which corresponds to the bathymetry of seafloor, can be used to calculate the xyz coordinates of the points that fall on the line. As the AUV moves, these

points will come in the illuminated region of the image; the RGB color values of the point can be identified based on the motion of the AUV.

### *B. Data analysis workflow*

For processing, the seafloor is divided into sections of 10m length, processed separately and the results are compiled. The workflow for processing each section is shown in Fig. 3. Visual data is classified into sections of crust, nodule and sediment, as described in section III-A to calculate the percentage cover of exposed crust. The acoustic measurements over non-crust regions are discarded and reflections are processed to make thickness measurements, as described in section III-B. These thickness values are extrapolated to the crust areas and the results are integrated to calculate the total volume of crust in the region, as described in section III-C.

## III. Algorithms

### *A. Seafloor classification*

The different seafloor types present in the survey area can be classified into continuous Mn-crust deposits, Mn-nodules and sediments [6]. Examples of each type are shown in Fig. 4.

In terrestrial applications, researchers have used Support Vector Machine (SVM) for classifying 3D point clouds [29]. Although neural networks are widely used in image classification tasks [30], [31], SVM was found to perform better with a small number of well defined classes and large training datasets [32], [33].

The authors built a SVM classifier with a polynomial kernel for identifying Mn-crust from seafloor bathymetry and colour maps [34], [35]. In order to make the classification scale to large areas, the seafloor was sampled into uniform sections called kernels and classified, reducing the processing times to be linearly proportional to the area of seafloor being classified. Two datasets (see Table III for details) were selected as training and testing, and cross validation sets to ensure that robust classification is achieved.

Each kernel is an independent 3D point cloud with each point described by its features (see Table II) derived from colour (RGB) and location (xyz) values, and has no overlap with adjacent kernels.

Bathymetric features describe the shape of the point cloud. The standard deviations in the vertical direction is a measure of the spread of the point cloud ($f_2$). The slope of the seafloor,

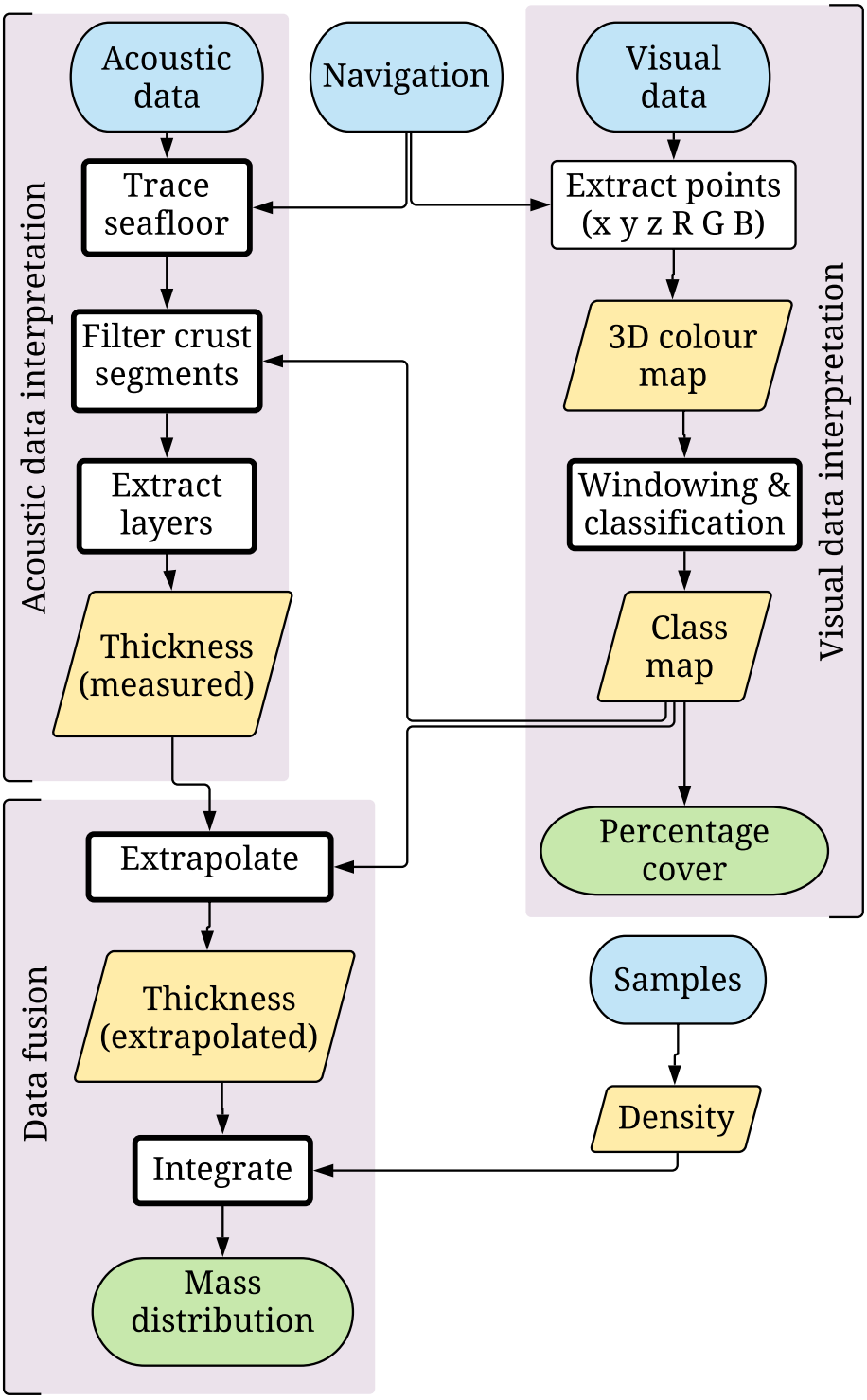


Fig. 3. Flowchart of data processing framework. Contributions of this paper are highlighted in bold outlines.

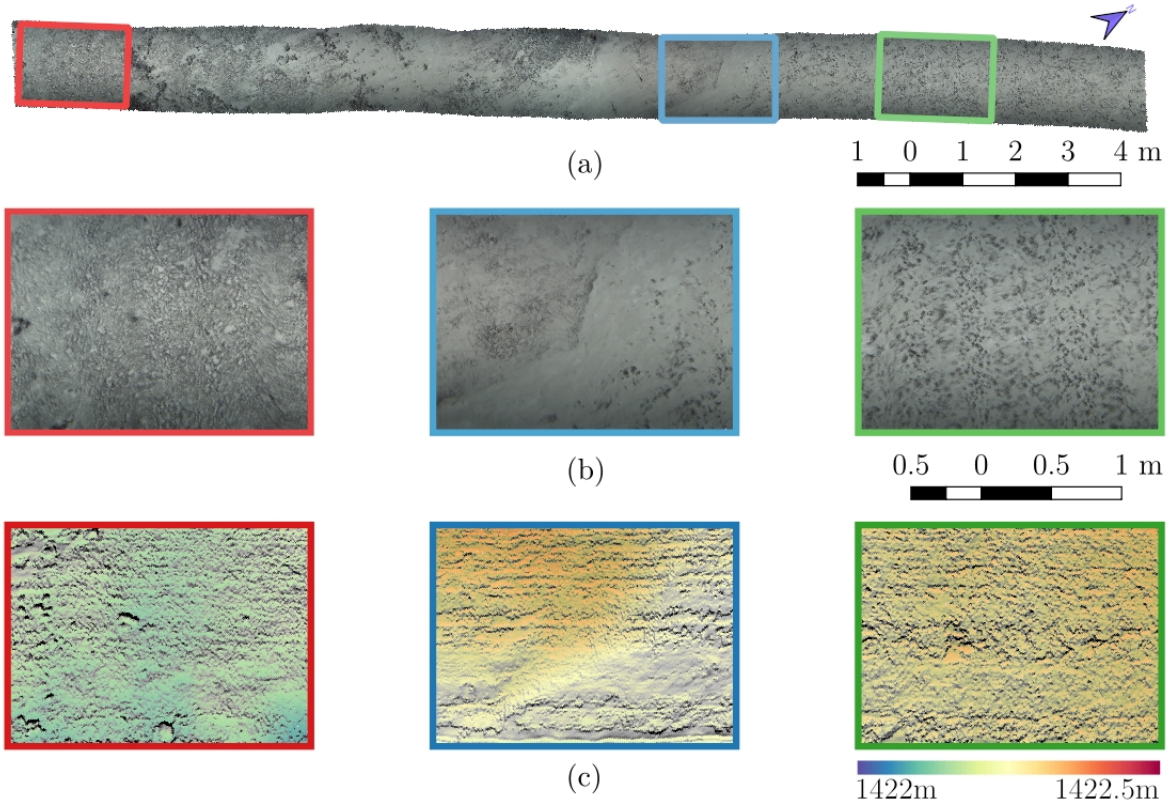


Fig. 4. Different types of seafloor present in the area. (a) Top view of a 21 m section, with insets showing different types. (b) Detailed views of each type. (c) Bathymetric maps. The frames are colored as follows: (Red) Continuous Mn-crust deposits. (Blue) Sediment covered areas. (Green) Nodules of varying sizes.

independent of the direction it is facing is represented by $f_1$ (measured as the altitude angle or elevation angle) and is calculated as the deviation of the normal of the seafloor $\mathbf{N}$.

$$f_1 = 90 - \cos^{-1}(\mathbf{N} \cdot \mathbf{V}) \tag{1}$$

where $\mathbf{V} = [0, 0, -1]^T$ is the unit vector along Z axis facing away from the seafloor.

The seafloor is relatively smooth in sediment covered areas and is more rough for crusts and nodules. This surface roughness is captured in two features, as defined in the ISO 4287:1997 standard, mean and standard deviation of the deviation from the plane of the kernel in the normal direction. Assuming that the kernel consists of n points, with each point $i$ being $(x_i, y_i, z_i, R_i, G_i, B_i)$, the deviation of each point can be calculated as

TABLE II

FEATURES CALCULATED WITHIN EACH KERNEL (BOLD FONT INDICATE THE FEATURES CHOSEN FOR USE IN THE FINAL CLASSIFIER BASED ON THE $F_1$ SCORES CALCULATED, SEE FIG. 7)

| Bathymetric Features | | Image Features | |
|---|---|---|---|
| $\boldsymbol{f_1}$ | **Slope** | $f_5$ | Luminosity mean |
| $f_2$ | Vertical standard deviation | $\boldsymbol{f_6}$ | **Luminosity standard deviation** |
| $\boldsymbol{f_3}$ | **Roughness mean** | $\boldsymbol{f_7}$ | **Luminosity entropy** |
| $\boldsymbol{f_4}$ | **Roughness standard deviation** | $\boldsymbol{f_8}$ | **Red intensity mean** |
| | | $f_9$ | Green intensity mean |
| | | $\boldsymbol{f_{10}}$ | **Blue intensity mean** |
| | | $\boldsymbol{f_{11}}$ | **Red intensity standard deviation** |
| | | $f_{12}$ | Green intensity standard deviation |
| | | $\boldsymbol{f_{13}}$ | **Blue intensity standard deviation** |

$$h_i = |\mathbf{N} \cdot [x_i, y_i, z_i]^T| \tag{2}$$

$f_3$ and $f_4$ are then calculated as the mean and the standard deviation of all the points within the kernel respectively.

Image features represent the features calculated from the colour of the seafloor. The simplest image features include the mean RGB values of the kernel ($f_8$, $f_9$ and $f_{10}$) and their standard deviation ($f_{11}$, $f_{12}$ and $f_{13}$). Since crusts and nodules appear darker than the sediment areas, a luminosity image of the kernel is constructed. Luminosity of a point $i$ is a measure of brightness of the point and can be calculated as

$$I_i = 0.21R_i + 0.72G_i + 0.07B_i. \tag{3}$$

The mean and standard deviation of luminosity for each kernel are calculated as $f_5$ and $f_6$ respectively. Entropy ($f_7$) is calculated from the luminosity image using the below equation.

$$f_7 = -\sum_j P(I_j) \log(P(I_j)) \tag{4}$$

where $P(I_j)$ is the probability that a random point $j$ will have a luminous intensity $I_j$.

The normalised values of all features can be compared using Fig. 5, where a kernel size of 10 cm edge length was found to be appropriate for discriminating between the different types of seafloor.

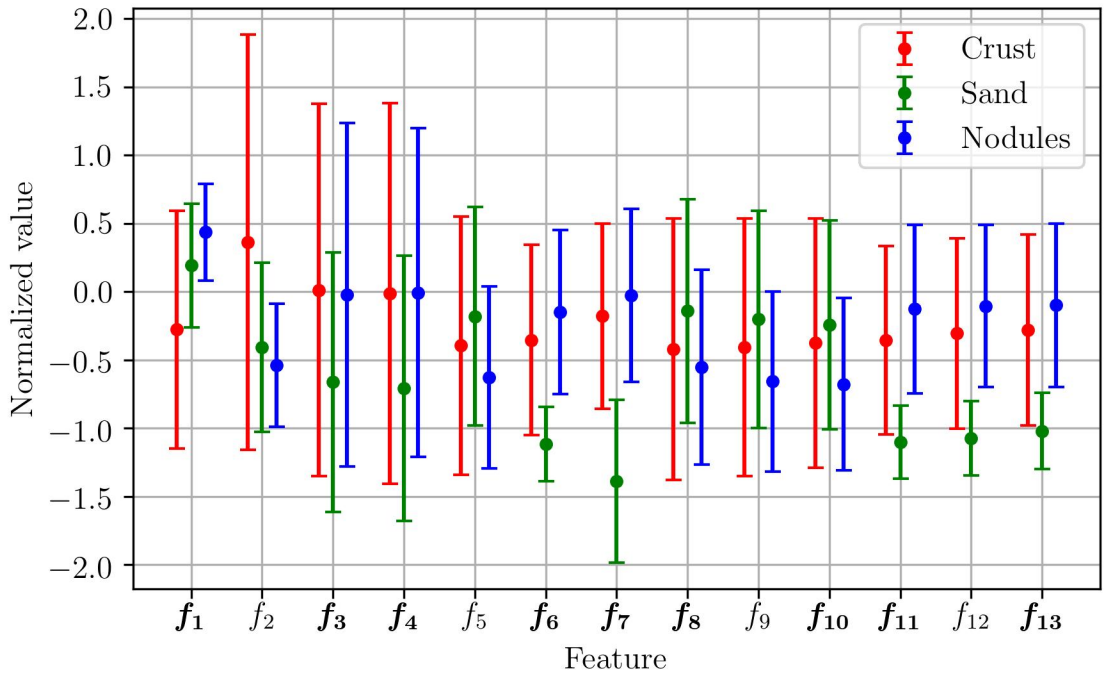


Fig. 5. Features used and their variation w.r.t. seafloor types. The values are normalized to approximately zero mean and unit variance across the whole training data for a kernel size of 10 cm. The bold font indicates features chosen for use in the final classifier based on the $F_1$ scores calculated, see Fig. 7.

In order to identify the optimal feature vector, optimize the hyper-parameters and train the classifier, two datasets are selected and manually labelled. A summary of the two datasets is shown in Table III. Dataset 1 consists of 58860 kernels and dataset 2 consists of 44830 kernels. The training data was constructed by randomly selecting 5000 kernels from dataset 1. The testing data for the classifier, whose results were used to tune the SVM, was constructed by randomly selecting a different set of 5000 kernels from dataset 1. The entire dataset 2 was used as the independent cross validation (CV) dataset and was used in the final step for selecting the best performing feature set.

Fig. 6 shows the confusion matrix of the classifier after optimization, where the crust kernels were double weighted during training to ensure the algorithm prioritises identifying Mn-crusts. The final performance was measured using the $F_1$ score [31], [36]. The feature set with the best classification performance was identified by doing an extensive search under three categories - image features only ($C_1$), bathymetric features only ($C_2$) and a combination of both image and

TABLE III

STATISTICS OF MANUALLY LABELLED DATASETS USED IN BUILDING THE SVM CLASSIFIER.

| Dataset | 1. Training and testing | 2. Cross validation |
|---|---|---|
| Dive number | BSA038 | BSA031 |
| Collected on | 2017 January 21 | 2016 January 24 |
| Crust area ($m^2$) | 140 | 179 |
| Sediment area ($m^2$) | 164 | 107 |
| Nodules area ($m^2$) | 285 | 162 |

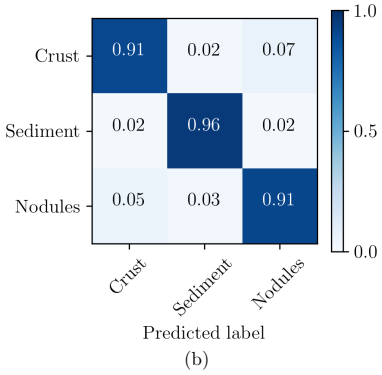


Fig. 6. Confusion matrix of classifier after optimisation.

bathymetric features ($C_3$). Feature vectors from $C_3$ performed better than others. Fig. 7 shows the accuracy values for the best two classifiers for each feature vector length with the CV accuracy plotted alongside. The classifier $\zeta_9$, with 9 features ($f_1$, $f_3$, $f_4$, $f_6$, $f_7$, $f_8$, $f_{10}$, $f_{11}$, and $f_{13}$), has both the highest CV scores of 90.0% accuracy and 87.7% $F_1$-score. This feature vector was selected for the SVM classifier and is highlighted in bold in Fig. 7. The decision boundary of the classifier $\zeta_9$ shows that crust is more prevalent in steeper areas. The mean roughness value is higher than the standard deviation of roughness for nodules indicating an undulating texture.

The classifier was further tuned by optimizing the hyper-parameters which influence the SVM decision function. Values were optimized using a random search over a large range of parameter values followed by an extensive grid search in the vicinity of the best performing parameter values [37].

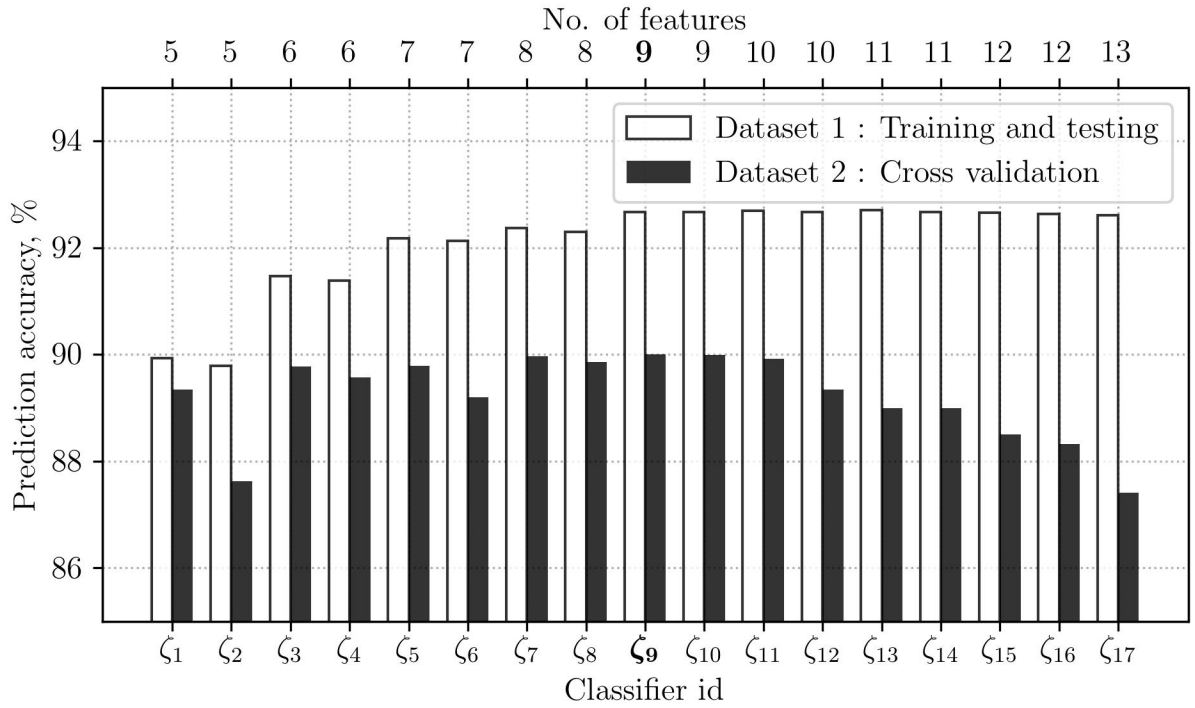


Fig. 7. Performance of the feature vector size on classification. Beyond 7 features, increasing the number of features increases scores by a minimal amount. However, on cross-validation, the higher results turn out to be due to overfitting. The selected classifier ($\zeta_9$) is highlighted.

### *B. Acoustic data interpretation*

Acoustic reflections made over seafloor sections classified as crust are used to estimate a thickness value [38]. The acoustic measurements are corrupted by noise generated by scattering, multi-path reflections, and local inclusions in the crust layer. In order to identify a continuous layer of Mn-crust from successive measurements, the algorithm carries out filtering of individual pulses, extracting signal boundaries, re-framing the signal into a distance based grid, and identifying secondary reflections to calculate thickness.

Initially, each recorded signal is filtered by removing the spectral components that fall away from the transmitted frequency of 200 kHz. In extracting signal boundaries, the signal region of interest is identified using binary thresholding using Otsu's method [39] to identify the first reflection, i.e. the top surface of the seafloor.

In the third step, the reflections are bundled into a single image frame, with adjacent signals lined up with their first reflection matching and subsequent values as pixel intensities below. The

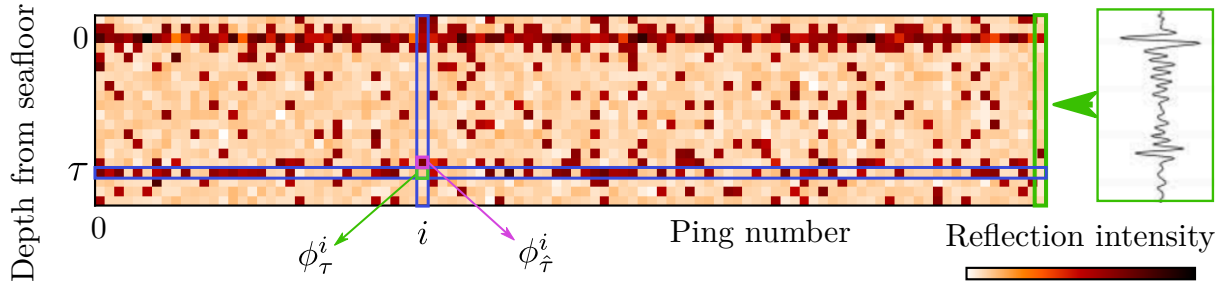


Fig. 8. Illustration showing acoustic thickness estimation. The reflections are arranged as an image aligned w.r.t. the top reflection. A cost function is calculated for each potential thickness (see (5))

signals are sampled into a uniform 2D grid. An illustration is shown in Fig. 8, where darker colours indicate stronger reflections. The image is filtered using a median filter in order to reduce noise. The signal intensities are then corrected for attenuation in crust.

Since the top surface has been identified as Mn-crust by the SVM classifier, a near continuous secondary reflection is assumed to exist and the best candidate is selected using an integral function that calculates the strength of reflections at each distance from the top surface. The entire acoustic frame is denoted as $\Phi$ and an individual point in the image as $\phi^i_\tau$, where $i$ denotes the X coordinate (ping number) and $\tau$ denotes the Y coordinate (depth from seafloor). A cost function is calculated for each potential thickness value of $\tau$ as shown in (5).

$$\Gamma_\tau = -\sum_{i \in X} |\phi^i_{\hat{\tau}}| \tag{5}$$

where $\phi^i_{\hat{\tau}}$ is the point with highest intensity within a threshold distance to $\tau$, for each ping $i$. For example, in Fig. 8, the point directly above $\tau$ is used ($\hat{\tau} = \tau - 1$). This is done to account for minor local variations of thickness within the layer. The mean thickness is identified as the $\tau$ having the lowest cost $\Gamma_\tau$ and the secondary layer, which is the crust-substrate interface, is calculated as $\phi^i_{\hat{\tau}}$ , for each ping $i$. Thus the thickness becomes

$$t_i = \hat{\tau}_i. \tag{6}$$

This will result in a thickness value which is consistent over the range of several meters, yet accommodates for the local, minor variations in crust thickness.

### C. Data fusion and crust volume estimation

The thickness measurements made in the previous step lie along the 2D path where each acoustic ping struck the seafloor within the 1.5 m wide 3D map. Since the thickness of Mn-crusts are assumed to change gradually over the range of several meters, the measured thickness values are extrapolated into all crust kernels and the volume of crust present in the area is calculated by integrating over all kernels.

To extrapolate thickness measurements, for a kernel $i$, a window of influence $J_i$ is defined as the set of all kernels within a threshold distance $d_{th}$ from the centre of $i$ (set to 2 m). The number of kernels in set $J_i$ is calculated to be $N_{J^i}$ and the number of crust kernels is calculated to be $C_{J^i}$. Assuming $\hat{J}_i$ to be the set of all kernels inside $J_i$ where a thickness measurement is made, the thickness of the crust at $i$ is calculated as a weighted sum of thickness values of $\hat{J}_i$

$$t_i = \begin{cases} \frac{\sum_{j \in \hat{J}_i} w_j t_j}{C_{\hat{J}_i}} & \text{if } C_{\hat{J}_i} > 0 \\ 0 & \text{otherwise} \end{cases} \tag{7}$$

where $C_{\hat{J}^i}$ is the number of crust kernels within $\hat{J}_i$. The weight $w_j$ of each measurement $t_j$ is calculated as an inverse function of euclidean distance from kernel $j$ to kernel $i$ ($d_{ij}$).

$$w_j = 1 - \frac{d_{ij}}{d_{th}}. \tag{8}$$

The local percentage cover of exposed Mn-crust deposits ($\Psi_i$) about $i$ is calculated as

$$\Psi_i = \frac{C_{J^i}}{N_{J^i}} 100. \tag{9}$$

Using the density of Mn-crust ($\rho$) calculated from samples collected in the area, the local mass coverage per unit area of Mn-crust about $i$ can be calculated as

$$M_i = \frac{\rho \sum_{j \in J_i} t_j}{N_{J^i}}. \tag{10}$$

The window of influence $J_i$ is then moved to the next point where a thickness measurement was taken and the calculations are repeated, to estimate the distribution of crust along the entire mapped area.

TABLE IV

SUMMARY OF FIELD EXPERIMENTS CONDUCTED AT TAKUYO DAIGO SEAMOUNT IN THE NORTHWESTERN PACIFIC OCEAN.

| Vehicle | Number of dives | Lateral distance surveyed (m) | Observation speed (m/s) | Observation time (min) |
|---|---|---|---|---|
| Hyper-Dolphin (ROV) | 1 | 3636 | 0.15 | 312 |
| Boss-A (AUV) | 5 | 7217 | 0.1 | 931 |

## IV. ANALYSIS OF FIELD SURVEYS

Field trials of the system were conducted at the southern shoulder of Takuyo Daigo. In a span of over 5 years, several dives were made to depths between 1350 m and 1600 m below sea level. A summary of the dives is given in Table IV.

### *A. Continuous flat Mn-crust deposits*

The steps in analysing a seafloor section to estimate crust distribution are shown in Figs. 9 and 10. They show a seafloor section consisting of a flat continuous Mn-crust layer which is 6 m in length and 1.5 m in width. Fig. 9(a) shows the top view of the 3D reconstruction with the red dots showing the locations of acoustic measurements. Towards the right, a short vertical drop, seen in the reconstruction as a white vertical strip, is present where the crust breaks off and the broken slabs can be seen immediately afterwards. The acoustic reflections recorded by the probe are shown in Fig. 9(b). The classification results are shown in Fig. 9(c); other than a small section in the middle, all measurements are made over Mn-crust. A thickness value is calculated for points (red dots in Fig. 9(a)) which lie on kernels classified as crust as shown in Fig. 9(d). The horizontal axis of the plots represents the distance corresponding to the trace of the acoustic measurements on the seafloor. Due to the gimbals continuously orienting the acoustic probe so that the pulse is normal to the seafloor, the trace is longer than the length of the 3D reconstruction. The percentage cover calculated using (9) is plotted in Fig. 10(a). The graph shows the dip in coverage in the middle due to the sediment covered area. The estimated mass coverage is shown in Fig. 10(b), with $\sim 180\,kg/m^2$ of crust.

### *B. Sediment to nodules transition*

Fig. 11 shows a 12 m section that transitions from full sediment cover to full nodule cover. The acoustic signals also show a clear change from a weak top reflection in sediment covered

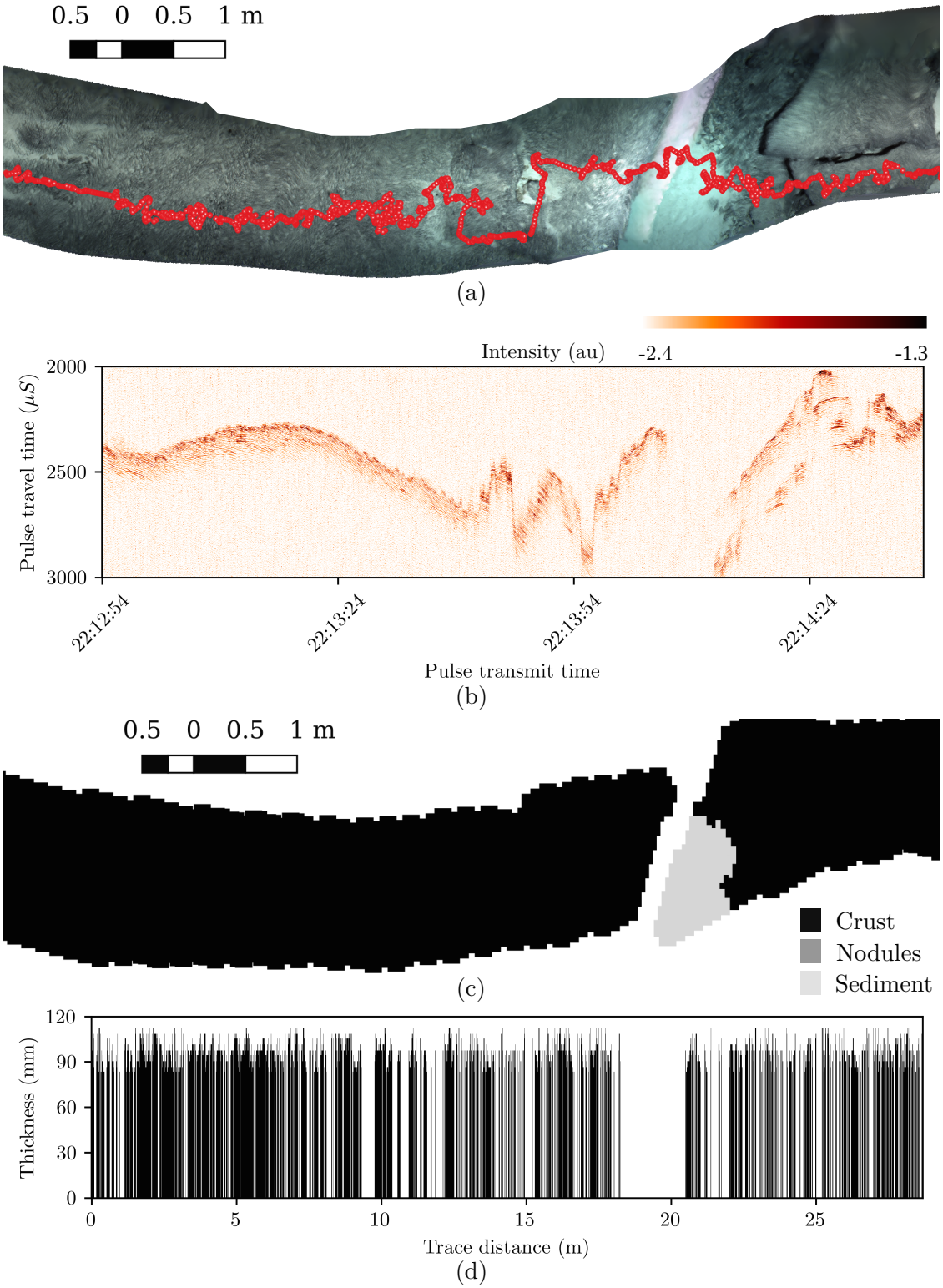


Fig. 9. Steps in processing the data collected over a flat crust section. The crust layer breaks towards the right and the broken pieces can be seen at the extreme right. A short vertical drop and a small section of sediment separates the two. (a) Top view of seafloor section with locations of acoustic measurements shown as dots. (b) Acoustic signals recorded. (c) SVM classification. (d) Estimated thickness values.

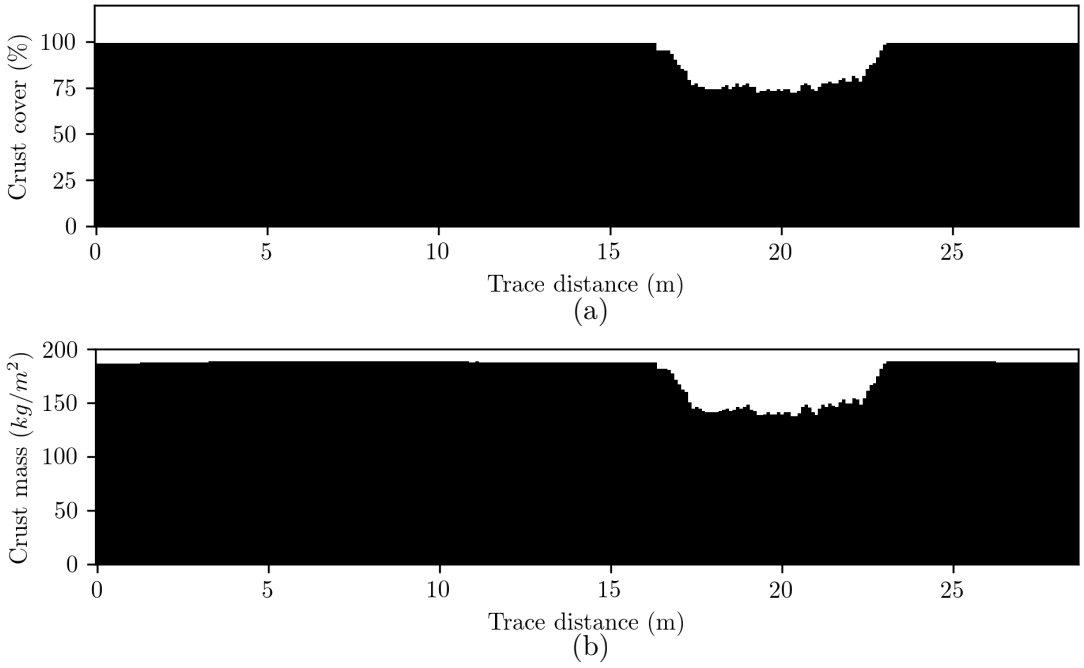


Fig. 10. The horizontal axis denotes the interpolated trace distance along the red dots in Fig. 9 and is significantly longer than the length of the seafloor section. (a) Percentage cover. (b) Mass coverage of crust.

areas to sharper reflections with change in the type of seafloor. Since no crust is present, no thickness values are calculated. However, in the acoustic reflections, a weak second reflection can be seen indicating the presence of a buried layer. It can be seen that some edge kernels are misclassified as crust due to the limitation of the color correction method used in generating the 3D maps. In the presented example, this creates a 2.7% error in the percentage cover estimates. However, since the acoustic data is collected along the middle of the transect, which is classified correctly as sand/nodules, no error in thickness measurements and final mass calculations are incurred.

### *C. Sediment covered flat Mn-crust near a ledge*

Figs. 12 and 13 shows a 12 m section of various types of seafloor. It is centred on a ledge of flat Mn-crust and partially covered by a layer of sediment. Below the ledge, a thick layer of sediment is visible, followed by broken slabs of Mn-crust. Since Mn-crusts are exposed partially, the coverage estimate oscillates between near zero and 80 %. Towards the left, the sparse and weak acoustic reflections indicate a sand layer and a second layer becomes clear where the crust

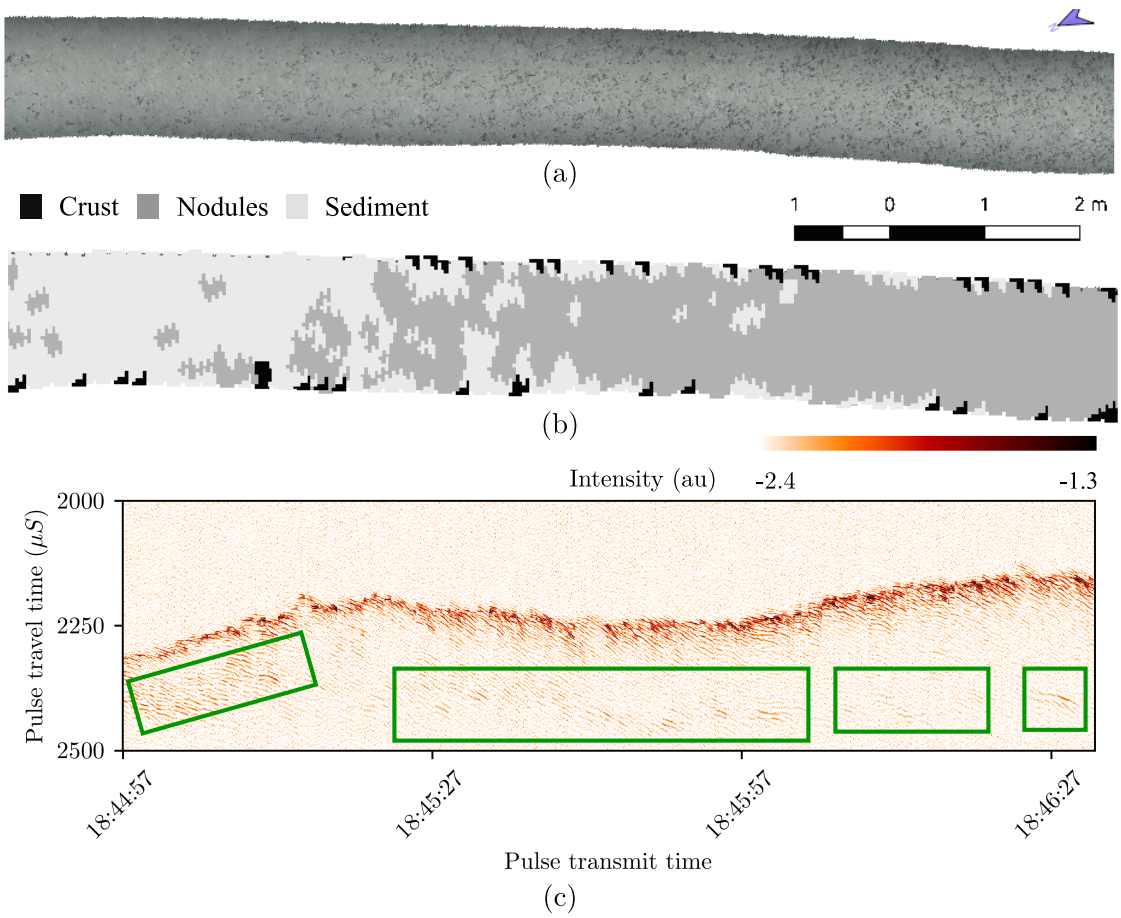


Fig. 11. A sediment section transitioning into a nodule section. Because no crust kernels were found, thickness values are not calculated. (a) Top view of the 3D reconstruction. The trace of acoustic measurements (see Fig. 9(a)) has been omitted for clarity of visualisation. (b) SVM classifier output. (c) Acoustic signals recorded by the probe, showing no consistent layer of crust. The image shows weak second layers of reflections in areas shown in boxes, presumably from a buried layer of crust.

is exposed. Towards the right, the seafloor is covered in nodules and it shows in the acoustic reflections as strong reflections, but with no secondary layer visible. To the left of the nodules, where a sand section of about 0.8 m is present, a secondary layer beneath the sediments is visible in the acoustic reflections; however, the type of the layer cannot be determined with the proposed techniques.

### *D. Compiled results from all dives*

The data collected from all the dives are analysed and combined, and the distributions for a 50 cm edge window are shown in Figs. 14-17. Since the ROV transects followed a crust layer, the results show a high percentage cover throughout. These four transects were mapped during a

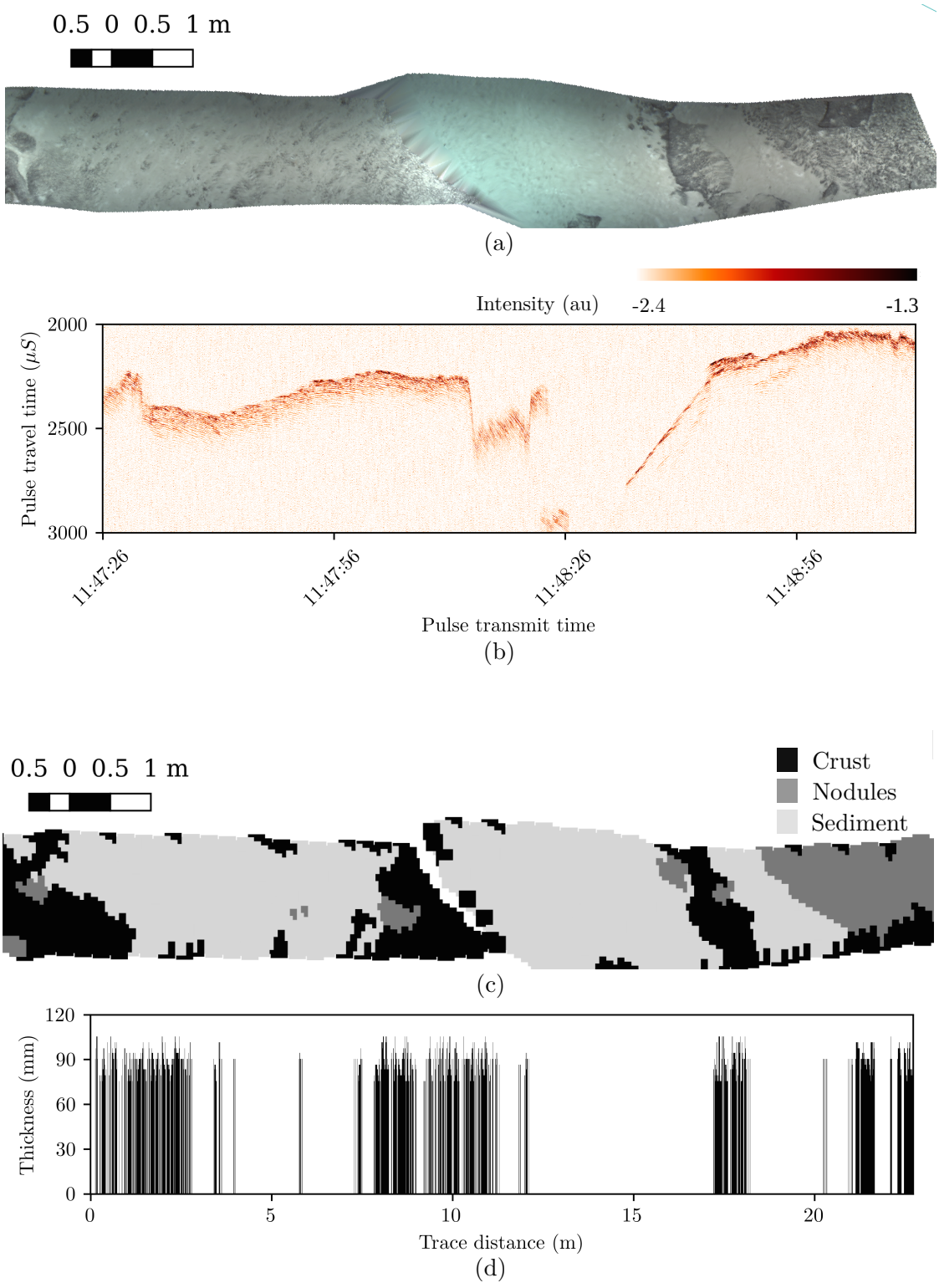


Fig. 12. Seafloor section containing a variety of types. Towards the left, the layer of crust is partially covered by sediment and gets broken in the middle. Farther to the right, the sections are covered by nodules. (a) Top view of seafloor section. (b) Acoustic signals recorded by the probe. (c) SVM classification of the seafloor section. (d) Thickness values estimated.

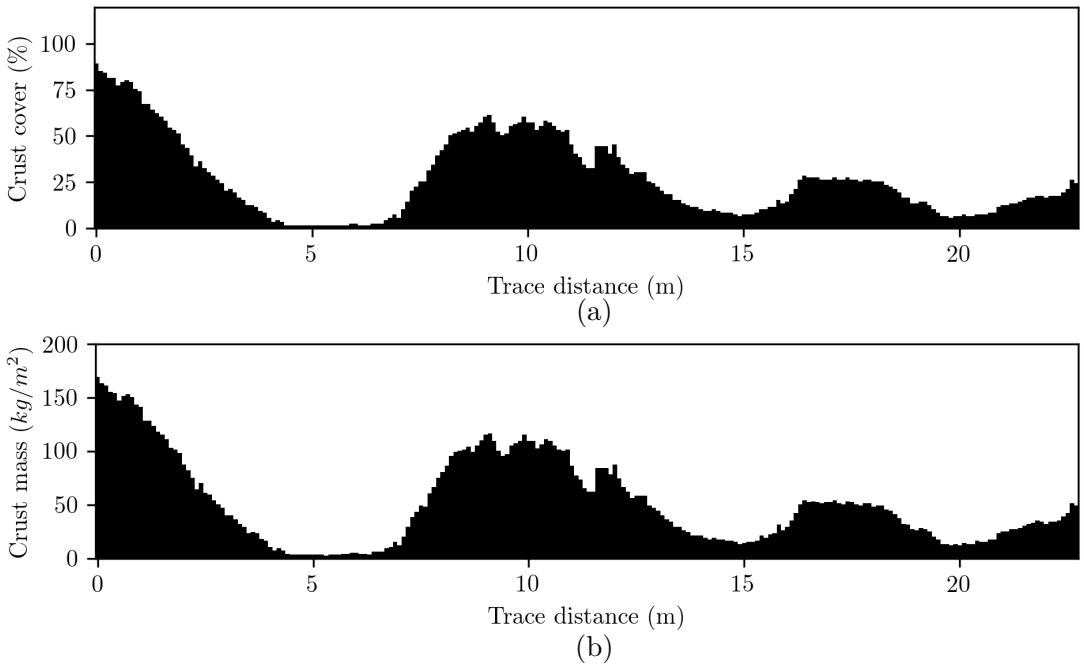


Fig. 13. Analysis results from the seafloor patch with different classes shown in Fig. 12. (a) Percentage cover of crust. (b) Mass coverage of crust. Towards the left side, although it is nearly 100% covered by crust, the layers are thin and hence the mass coverage is only about 75% of the maximum coverage expected in the area.

single dive and are indicated using green arrowheads. The remaining transects, mapped by AUV shows a varying landscape that can have anywhere between zero and one hundred percent crust coverage. It can be seen that the lower sections of the seamount, which are also steeper, have a high crust coverage. In some areas, the cover is seen to vary rapidly. The section marked by ★ has flat continuous Mn-crust deposits in the upper section, whereas the lower section, only 10 m away, shows a sediment covered seafloor. This high variability in the seafloor classes indicate the need for a continuous measurement system in order to assess the crust volume accurately. Locations A and B in Fig. 14 are intersects of ROV and AUV transects, with close-up views in Fig. 15 showing consistency between the transects. Crossing A is a sand covered crust area (exposed crust can be seen to the right and top of the intersection) with some rocks. Crossing B is covered with nodules of various sizes.

The thickness values measured and the samples collected from the area are shown in Fig. 16. The relative abundance of crust in the upper and lower sections of the map and the lack of crust in the central regions is observed. The thickness varies from about 40 mm to a maximum of

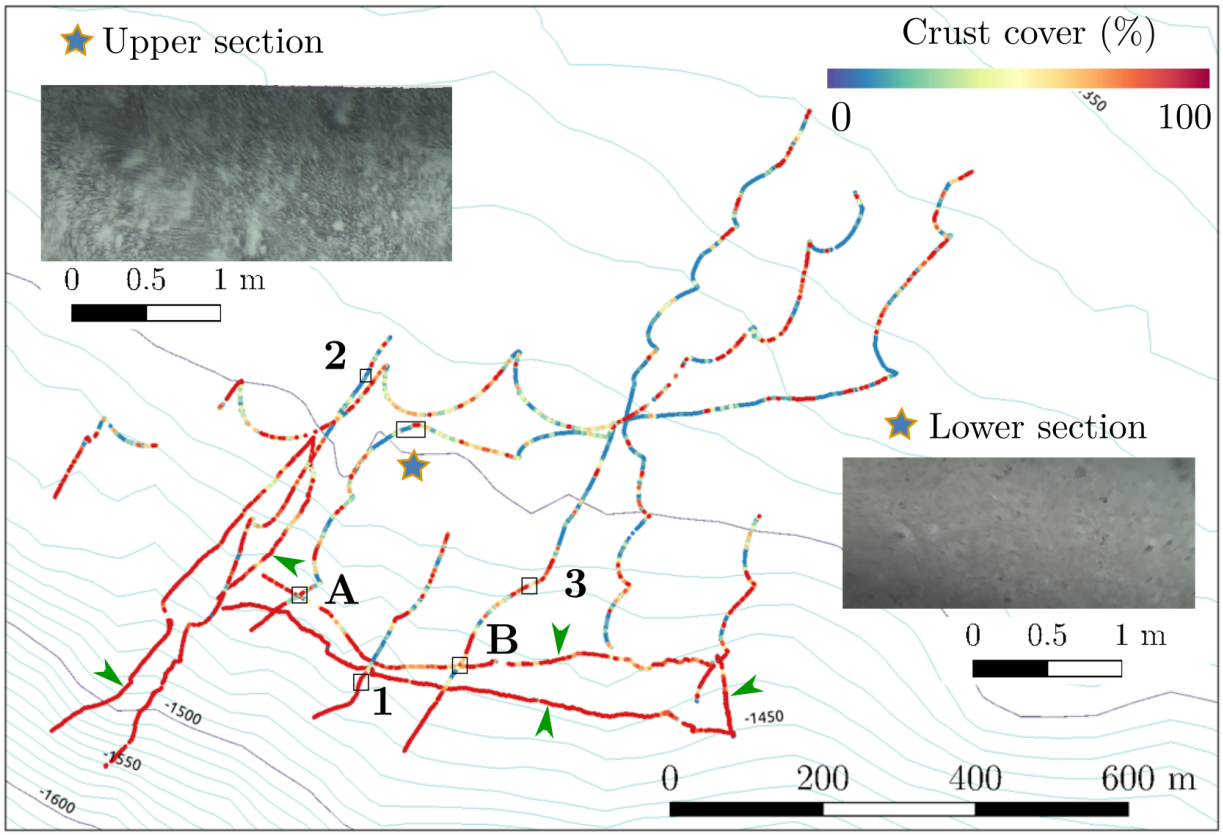


Fig. 14. Percentage cover of Mn-crust along mapped transects. The 4 ROV transects (shown by arrows) have a higher % cover as regions with exposed crusts were followed manually by the ROV pilots, whereas the AUV used for all other transects followed pre-planned trajectories. Crust coverage can vary rapidly such as in the area marked by ★; very different landscapes only 10 m apart (3D maps shown in insets).

114 mm, with a mean thickness of 69.6 mm. A total of 26 samples were collected in the past in the area covered; their locations are shown as green triangles. Although there is no exact overlap between the samples collected and the surveyed regions, 7 samples are within 10 meters of the transects. These samples, shown as red triangles are used for further analysis for comparing the results of the present survey with sampling based methods in section IV-E.

The final volumetric estimates are shown in Fig. 17, which shows the unit crust coverage for every part of the mapped regions. The results vary from zero up to a maximum of 204 kg/m$^2$. As observed from Figs. 14 and 16, the lower, steeper sections of the seamount contains maximum coverage of crusts, even though the coverage can vary abruptly in a short range of a few tens of meters.

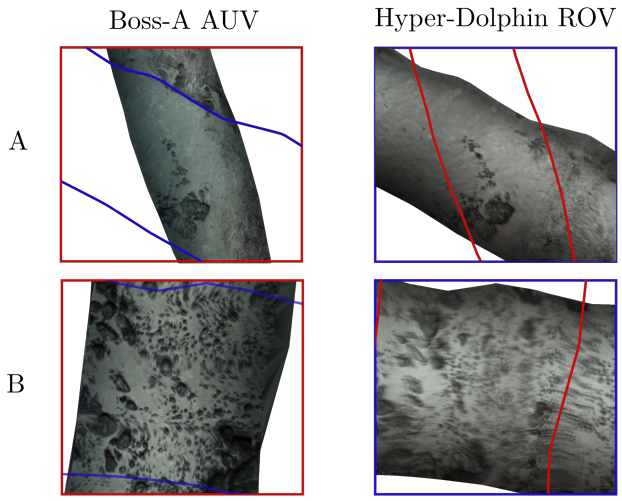


Fig. 15. Two locations where the transects intersect are selected for inter-comparison between AUV and ROV collected data (See Fig. 14 for the locations). The blue outline shows the ROV transects and the red outline indicates the AUV transects.

### *E. Discussion*

Quantitative estimates of Mn-crust abundance were obtained over large areas using the instruments and methods described. A summary of the results along with the variability and estimates of uncertainty for each measurement is provided in Table V. The variability is calculated as the one-sigma deviation from the mean value. The uncertainty is estimated as the error in measurements on the mean and variability values.

The sources of error in the measurements are propagated as systematic errors depending on the thickness, the density of crust, area and the classification. The 3D mapping system has an 1-sigma uncertainty of 9.17 % affecting the total mapped area. The thickness measurements are subject to a 6.1 % variability in the velocity of sound ($2932 \pm 179\, m/s$) in Mn-crusts [19]. The percentage cover has 10 % uncertainty from classification (cross validation accuracy - see section III-A). In calculating the total amount of Mn-crust present in the area, a 1.9 % variability in the density of crust ($1920 \pm 36\, kg/m^3$) is also considered [19], resulting in a total uncertainty of 27.2 %. It is estimated that there is 870 t of Mn-crust in the mapped area, with an uncertainty of 237 t. Error in mass coverage is calculated to be 18 % and the calculations show the amount of crust per unit area to be 69.6 kg/m$^2$ with an uncertainty of 12.5 kg/m$^2$. However, particularly notable is the variability of $59.7(\pm 10.7) kg/m^2$, which is 85.8% of the mean value. This is consistent with the observation that crust deposits are highly variable and therefore require continuous measurements

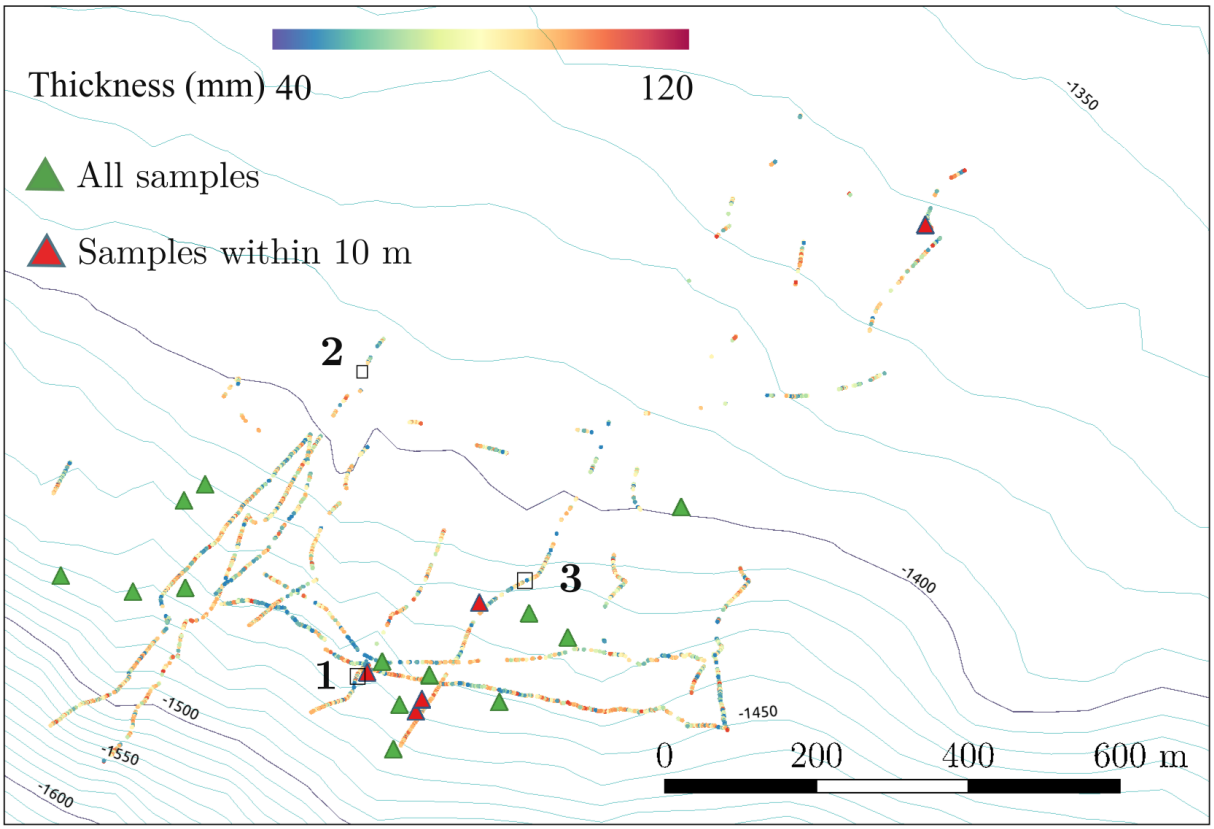


Fig. 16. Thickness of Mn-crust along mapped transects. The thickness is higher in deeper and steeper sections of the seamount (left bottom area). The samples collected from the visible area and the samples which are close to the mapped area are shown as green and red triangles respectively.

to accurately map their distribution and indicates that high resolution measurements are required for accurate portrayal of crust distribution and inventory survey.

A comparison of the results is made with estimates made using only samples taken within 10 m of the mapped region, which show a mean thickness of 63.3 mm with a standard deviation of 29.5 mm. A total of 7 samples are selected, which are collected from 5 locations as indicated in Fig. 16. The limited number of samples constitute a large statistical error of 37.8 % in sample thickness measurements. Since percentage cover cannot be calculated from samples, the estimates made in the previous step are used to illustrate the advantages of continuous measurements. It can be seen from Table V that the final estimated crust mass per unit area and the total amount of crust in an area equal in size to the mapped area has an uncertainty of 49.7 % and 58.9 % respectively.

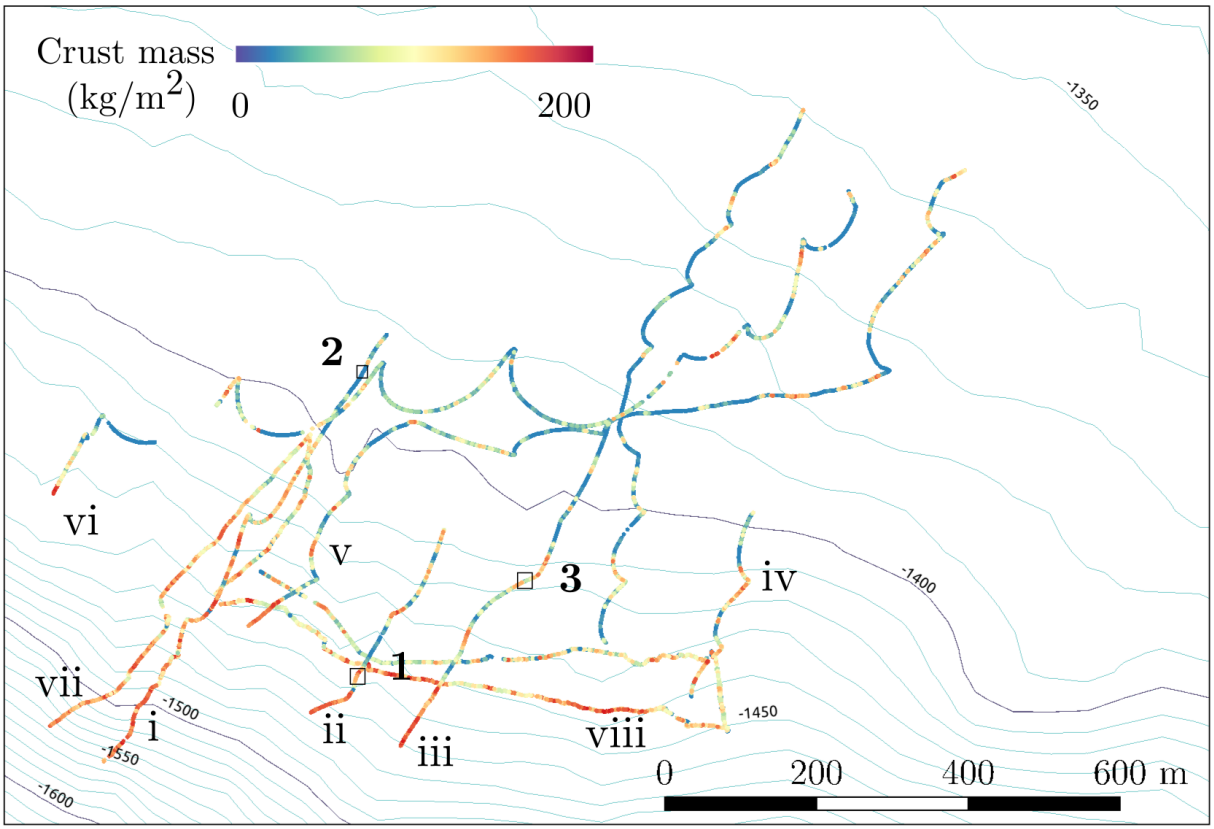


Fig. 17. Final volumetric coverage estimate along mapped transects. The results vary from nil to 204 kg/m$^2$, with the maximum crust coverage found in the steeper lower sections of the mapped region.

The high uncertainty in surveys based on sampling, as compared to AUV surveys, arises due to the significantly smaller number of measurements. In acoustic surveys from an AUV, there are over one million measurements and thus the statistical error is negligible. Only the 6.1 % systematic error, due to the variability in the speed of sound, needs to be considered. On the contrary, the thickness of physically recovered samples can be measured with high accuracy, making the systematic error almost zero. Nevertheless, the statistical error is high and can be reduced only by increasing the number of samples in the given area. Producing an uncertainty less than the systematic error in the acoustic measurements require a minimum of 268 samples to be collected for an equivalent surveyed area. Since sampling using ROVs takes approximately 40 min to 1 h [2], collecting so many representative samples is not practical. Furthermore, the continuous local variability of crust cover indicates that pointwise sampling alone is not suitable

TABLE V

ESTIMATED MN-CRUST AT TAKUYO DAIGO SEAMOUNT MEASURED ALONG A TOTAL TRANSECT LENGTH OF 10.9 KM (SEE TABLE IV FOR SURVEY DETAILS), WITH UNCERTAINTY VALUES IN BRACKETS. THE VARIABILITY OF ESTIMATED VALUES INDICATES THE CONTRASTING NATURE OF THE MN-CRUST DEPOSITS. AN INDICATIVE ESTIMATE USING ONLY SAMPLES COLLECTED FROM THE SAME AREA IS COMPARED.

| Parameter | Proposed method | | Samples N=7 | |
|---|---|---|---|---|
| | Mean ($\pm\sigma$) | Variability ($\pm\sigma$) | Mean ($\pm\sigma$) | Variability ($\pm\sigma$) |
| Total area mapped ($m^2$) | 12,510 ($\pm$1150) | - | - | - |
| Percentage cover (%) | 52.0 ($\pm$5.20) | $\pm$39.0 ($\pm$3.90) | - | - |
| Thickness of crust ($mm$) | 69.6 ($\pm$4.25) | $\pm$18.7 ($\pm$1.14) | 63.3 (23.9) | 29.5 (11.2) |
| Crust per unit area ($kg/m^2$) | 69.6 ($\pm$12.5) | $\pm$59.7 ($\pm$10.7) | 63.2* ($\pm$31.4)* | 22.1* ($\pm$10.1)* |
| Amount of crust (t) | 870 ($\pm$237) | - | 791* ($\pm$466)* | - |

* Visual mapping data for area estimates is used to calculate this value.

for accurate survey of Mn-crust distribution.

In order to study the spatial distribution of Mn-crust over the scale of hundreds of metres, crust per unit area and its variance for each transect (see Fig. 17 for transect numbers) is compared in Fig. 18. These transects are roughly parallel in most places and are spaced between 100 to 250 m in the lower sections. The bar charts to the right show estimates made by randomly selecting a fixed number points, equally from each transect, to simulate sampling where the total number of points considered is shown. The error bars indicate the systematic error for the full data, and the standard deviation of 50 iterations for each random selection of point location. The systematic error is not shown in the random point samples to illustrate the level of uncertainty that would be expected if an equivalent number of samples was recovered. A larger number of points provide a more representative estimate of the crust coverage where the statistical error levels become comparable to the systematic errors in the proposed method after 200 random points. Even with 200 locations sampled, which would take approximately 8 days of bottom time

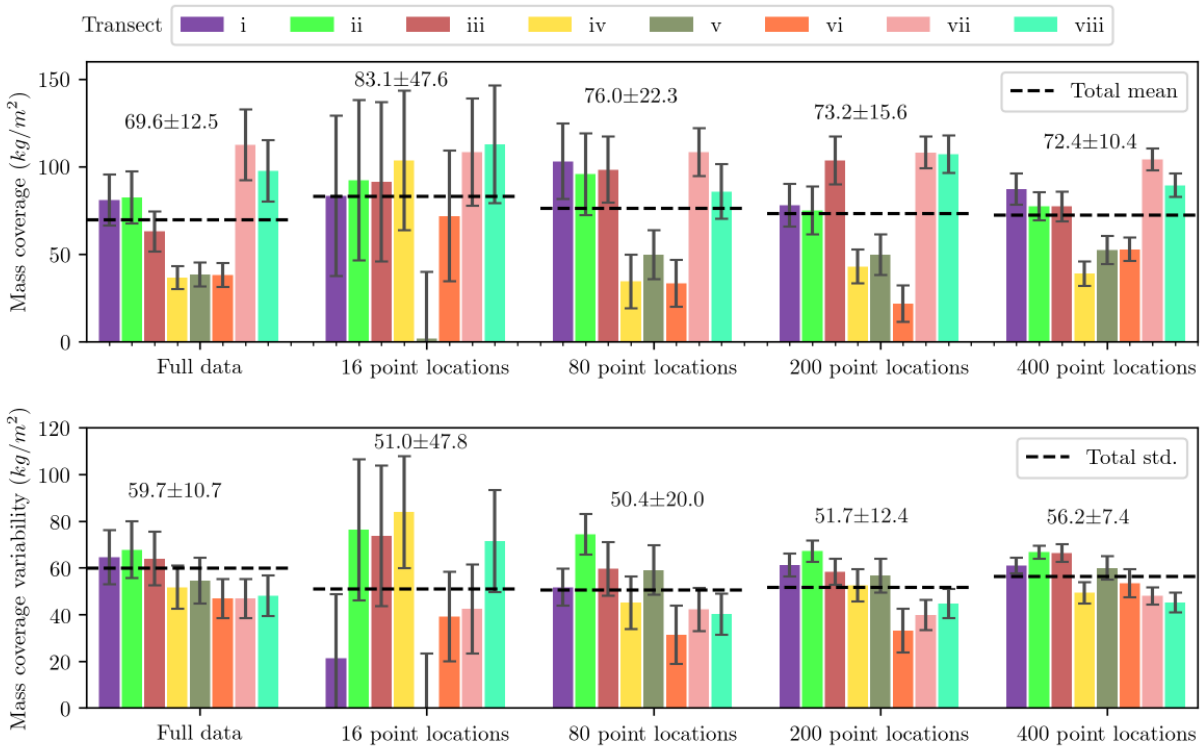


Fig. 18. Mass coverage of each transect shown in Fig. 17 and its variability. This is compared with a hypothetical sampling scenario, by randomly selecting points from the surveyed data. Mean value and error for each dataset is written above the bars. Variations among transects shows that extrapolating the results from a single transect to the whole area can result in erroneous estimates. The error values indicate that $>200$ random samples are required for getting an accuracy comparable to the proposed method.

for ROV sampling, the spatial variability still influences the estimates (e.g transect iii), indicating further sampling is required to capture the variability between adjascent transects. The variation in estimates among transects indicates that extrapolating results from a single transect over the entire mapped area can lead to highly inaccurate results. Multiple surveys at different locations are required to accurately estimate crust coverage and volume.

## V. Conclusion

- In-situ measurements of the distribution of Mn-crust in hectare scale regions has been demonstrated for the first time by using machine learning tools to analyze visual 3D maps and acoustic sub-bottom sonar measurements. The results are combined to calculate the total mass and distribution of the Mn-crust in the region. The measurements were validated

using samples collected from the survey area, which indicated a comparable total volume of crust.

- SVM methods can achieve a high level of classification accuracy (90%), where it has been demonstrated that combining both shape and visual features improves the performance over classifiers that consider only shape or visual features. Furthermore, this study showed that using too many features leads to overfitting, and that a relatively small number of combined features has better generalisation.
- The proposed method is advantageous over sampling with a nearly 50 % lower uncertainties in crust estimates. It is shown that it is not practical to achieve a similar uncertainty level using sampling and video surveys since $>$200 samples would be required. Also, the proposed method avoids the inherent biases of sampling towards samples that are easy to collect, and not characterising regions with no samples, such as nodules and sediments.
- The surveyed region of the Takuyo Daigo seamount has an average Mn-crust distribution of 69.6 kg/m$^2$ for a 12,510 m$^2$ mapped region, with occurrence ranging between 0 and 204 kg/m$^2$. The region had a variability in distribution of 85.8%, indicating that continuous measurements are needed in order to accurately characterise Mn-crust distribution.

## ACKNOWLEDGMENT

The authors thank the Hyper-Dolphin team, R/V Natsushima crew, R/V Yokosuka crew, and R/V Kairei crew, Japan Agency for Marine-Earth Science and Technology (JAMSTEC) during the NT13-13, KR16-01, and YK17-23C cruises. This work was supported by the Japanese Ministry of Education under the Program for the Development of Fundamental Tools for the Utilization of Marine Resources.

## REFERENCES

[1] M. Clark, R. Heydon, J. Hein, S. Smith, C. Smith, S. Petersen, E. Baker, and Y. Beaudoin, *Deep Sea Minerals: Cobalt-rich Ferromanganese Crusts, a physical, biological, environmental, and technical review*, E. Baker and Y. Beaudoin, Eds. Secretariat of the Pacific Community, 2013.

[2] A. Usui, K. Nishi, H. Sato, Y. Nakasato, B. Thornton, T. Kashiwabara, A. Tokumaru, A. Sakaguchi, K. Yamaoka, S. Kato, S. Nitahara, K. Suzuki, K. Iijima, and T. Urabe, "Continuous growth of hydrogenetic ferromanganese crusts since 17Myr ago on Takuyo-Daigo Seamount, NW Pacific, at water depths of 800-5500m," *Ore Geology Reviews*, 2016.

[3] A. Usui, I. J. Graham, R. G. Ditchburn, A. Zondervan, H. Shibasaki, and H. Hishida, "Growth history and formation environments of ferromanganese deposits on the Philippine Sea Plate, northwest Pacific Ocean," *Island Arc*, vol. 16, no. 3, pp. 420–430, sep 2007.

[4] T. Yamazaki, R. Sharma, and K. Tsurusaki, "Microtopographic analysis of cobalt-rich manganese deposits on a mid-pacific seamount," *Marine Georesources & Geotechnology*, vol. 12, no. 1, pp. 33–52, jan 1994.

[5] T. Yamazaki and R. Sharma, "Distribution characteristics of co-rich manganese deposits on a seamount in the central Pacific Ocean," *Marine Georesources & Geotechnology*, vol. 16, no. 4, pp. 283–305, oct 1998.

[6] G. He, W. Ma, C. Song, S. Yang, B. Zhu, H. Yao, X. Jiang, and Y. Cheng, "Distribution characteristics of seamount cobalt-rich ferromanganese crusts and the determination of the size of areas for exploration and exploitation," *Acta Oceanologica Sinica*, vol. 30, no. 3, pp. 63–75, 2011.

[7] J. R. Hein, K. Mizell, A. Koschinsky, and T. A. Conrad, "Deep-ocean mineral deposits as a source of critical metals for high- and green-technology applications: Comparison with land-based resources," *Ore Geology Reviews*, vol. 51, no. July, pp. 1–14, 2013.

[8] I. A. Yeo, K. Dobson, P. Josso, R. B. Pearce, S. A. Howarth, P. A. J. Lusty, T. P. L. Bas, and B. J. Murton, "Assessment of the Mineral Resource Potential of Atlantic Ferromanganese Crusts Based on Their Growth History, Microstructure, and Texture," *Minerals*, vol. 8, no. 8, p. 327, 2018.

[9] P. A. Lusty, J. R. Hein, and P. Josso, "Formation and occurrence of ferromanganese crusts: Earth's storehouse for critical metals," *Elements*, vol. 14, no. 5, pp. 313–318, 2018.

[10] M. M. P. Weydert, "Measurements of the acoustic backscatter of selected areas of the deep seafloor and some implications for the assessment of manganese nodule resources," *The Journal of the Acoustical Society of America*, vol. 88, no. 1, pp. 350–366, jul 1990.

[11] ——, "Measurements of the acoustic backscatter of manganese nodules," *The Journal of the Acoustical Society of America*, vol. 78, no. 6, pp. 2115–2121, dec 1985.

[12] P. A. Lusty and B. J. Murton, "Deep-ocean mineral deposits: Metal resources and windows into earth processes," *Elements*, vol. 14, no. 5, pp. 301–306, 2018.

[13] C. de Moustier, "Inference of manganese nodule coverage from Sea Beam acoustic backscattering data," *Geophysics*, vol. 50, no. 6, pp. 989–1001, jun 1985.

[14] B. Chakraborty, V. Kodagali, and J. Baracho, "Sea-floor classification using multibeam echo-sounding angular backscatter data: a real-time approach employing hybrid neural network architecture," *IEEE Journal of Oceanic Engineering*, vol. 28, no. 1, pp. 121–128, 2003.

[15] V. N. Hari, B. Kalyan, M. Chitre, and V. Ganesan, "Spatial Modeling of Deep-Sea Ferromanganese Nodules With Limited Data Using Neural Networks," *IEEE Journal of Oceanic Engineering*, vol. 43, no. 4, pp. 997–1014, oct 2018.

[16] T. Schoening, D. O. Jones, and J. Greinert, "Compact-Morphology-based poly-metallic Nodule Delineation," *Scientific Reports*, vol. 7, no. 1, pp. 1–12, 2017.

[17] M. M. P. Weydert, "Design of a system to assess manganese nodule resources acoustically," *Ultrasonics*, vol. 29, no. March, pp. 150–158, 1991.

[18] A. Usui and M. Someya, "Distribution and composition of marine hydrogenetic and hydrothermal manganese deposits in the northwest Pacific," *Geological Society, London, Special Publications*, vol. 119, no. 1, pp. 177–198 pp, 1997.

[19] B. Thornton, A. Asada, A. Bodenmann, M. Sangekar, and T. Ura, "Instruments and methods for acoustic and visual survey of manganese crusts," *IEEE Journal of Oceanic Engineering*, vol. 38, no. 1, pp. 186–203, jan 2013.

[20] A. Mehta, E. Ribeiro, J. Gilner, and R. van Woesik, "Coral reef texture classification using support vector machines," in *Proceedings of the Second International Conference on Computer Vision Theory and Applications*, no. Volume 2, Barcelona, Spain, 2007, pp. 302–310.

[21] M. D. Stokes and G. B. Deane, "Automated processing of coral reef benthic images," *Limnology and Oceanography-Methods*, vol. 7, pp. 157–168, 2009.

[22] A. Lüdtke, K. Jerosch, O. Herzog, and M. Schlüter, "Development of a machine learning technique for automatic analysis of seafloor image data: Case example, Pogonophora coverage at mud volcanoes," *Computers and Geosciences*, vol. 39, pp. 120–128, 2012.

[23] A. Friedman, "Automated interpretation of benthic stereo imagery," Ph.D. dissertation, The University of Sydney, 2013.

[24] T. Schoening, M. Bergmann, and T. W. Nattkemper, "Investigation of hidden parameters influencing the automated object detection in images from the deep seafloor of the HAUSGARTEN observatory," in *2012 Oceans*. IEEE, oct 2012, pp. 1–5.

[25] U. Neettiyath, T. Sato, M. Sangekar, A. Bodenmann, B. Thornton, T. Ura, and A. Asada, "Identification of manganese crusts in 3D visual reconstructions to filter geo-registered acoustic sub-surface measurements," in *OCEANS 2015 - MTS/IEEE Washington*. IEEE, oct 2015, pp. 1–6.

[26] Y. Nishida, K. Nagahashi, T. Sato, A. Bodenmann, B. Thornton, A. Asada, and T. Ura, "Autonomous Underwater Vehicle "BOSS-A" for Acoustic and Visual Survey of Manganese Crusts," *Journal of Robotics and Mechatronics*, vol. 28, no. 1, pp. 91–94, 2016.

[27] T. Sato, B. Thornton, A. Bodenmann, A. Asada, and T. Ura, "Towards real-time control of a double gimbaled acoustic probe for measurement of manganese crusts thickness," in *2013 IEEE International Underwater Technology Symposium, UT 2013*, 2013.

[28] A. Bodenmann, B. Thornton, and T. Ura, "Generation of High-resolution Three-dimensional Reconstructions of the Seafloor in Color using a Single Camera and Structured Light," *Journal of Field Robotics*, vol. 34, no. 5, pp. 833–851, dec 2017.

[29] K. Kusumam, T. Krajník, S. Pearson, T. Duckett, and G. Cielniak, "3D-vision based detection, localization, and sizing of broccoli heads in the field," *Journal of Field Robotics*, vol. 34, no. 8, pp. 1505–1518, 2017.

[30] M. S. A. C. Marcos, M. N. Soriano, and C. A. Saloma, "Classification of coral reef images from underwater video using neural networks," *Optics Express*, vol. 13, no. 22, p. 8766, 2005.

[31] M. Kubat, *An Introduction to Machine Learning*. Springer International Publishing Switzerland, 2015.

[32] R. Caruana and A. Niculescu-Mizil, "An empirical comparison of supervised learning algorithms," in *Proceedings of the 23rd international conference on Machine learning - ICML '06*. New York: ACM Press, 2006, pp. 161–168.

[33] D. L. Bongiorno, M. Bryson, T. C. L. Bridge, D. G. Dansereau, and S. B. Williams, "Coregistered Hyperspectral and Stereo Image Seafloor Mapping from an Autonomous Underwater Vehicle," *Journal of Field Robotics*, vol. 35, no. 3, pp. 312–329, may 2018.

[34] J. Unpingco, *Python for Probability, Statistics, and Machine Learning*. Cham: Springer International Publishing, 2016.

[35] F. Pedregosa, G. Varoquaux, A. Gramfort, V. Michel, B. Thirion, O. Grisel, M. Blondel, P. Prettenhofer, R. Weiss, V. Dubourg, J. Vanderplas, A. Passos, D. Cournapeau, M. Brucher, M. Perrot, and E. Duchesnay, "Scikit-learn: Machine Learning in Python," *Journal of Machine Learning Research*, vol. 12, pp. 2825–2830, 2011.

[36] S. V. Stehman, "Selecting and interpreting measures of thematic classification accuracy," *Remote Sensing of Environment*, vol. 62, no. 1, pp. 77–89, 1997.

[37] J. Bergstra and U. Yoshua Bengio, "Random Search for Hyper-Parameter Optimization," *Journal of Machine Learning Research*, vol. 1, pp. 281–305, 2012.

[38] U. Neettiyath, B. Thornton, M. Sangekar, K. Ishii, T. Sato, A. Bodenmann, and T. Ura, "Automatic Extraction of Thickness Information from Sub-Surface Acoustic Measurements of Manganese Crusts," in *OCEANS 2017 - Aberdeen*. IEEE, jun 2017, pp. 1–7.

[39] N. Otsu, "A threshold selection method from gray-level histograms," *IEEE Transactions on Systems, Man, and Cybernetics*, vol. 9, no. 1, pp. 62–66, 1979.

**Umesh Neettiyath** received his B.Tech degree in Electronics and Communication from the University of Calicut (2008) and his M.S. by Research in Engineering Design from Indian Institute of Technology Madras (2013). He is currently a Project Researcher at the Institute of Industrial Science at The University of Tokyo. His research interests include the design and development of field robotics systems for environmental observation. He is currently working on large scale data collection and analysis of manganese crust deposits using underwater robots.

**Blair Thornton** (M'07) received the B.Eng. degree in ship science and the Ph.D. degree in underwater robotics from The University of Southampton, Southampton, U.K., in 2002 and 2006, respectively. He is at present an Associate Professor at the the University of Southampton and also affiliated with the Ocean Perception Laboratory, Institute of Industrial Science, The University of Tokyo. His research interests involve the development of in-situ sensors and data processing techniques for integrated acoustic, visual, and chemical survey of marine minerals and environment monitoring. He is dedicated to fielding real systems in real environments and overcoming bottlenecks in the flow of information from data collection to human interpretation.

**Mehul Sangekar** (M'10) received the M.Sc. degree in underwater robotics and Ph.D. degree in ocean technology from The University of Tokyo, Japan, in 2010 and 2014, respectively. He is working at present as a project researcher at the Thornton Lab, Institute of Industrial Science, The University of Tokyo. Currently, he works on techniques for intelligent, multi-layer resolution mapping of the seafloor using autonomous underwater vehicles. He is also working on developing algorithms for analysis of high resolution seafloor bathymetry and correlating it with other measured seafloor parameters.

**Yuya Nishida** received a Ph.D. in engineering from the Kyushu Institute of Technology in 2011. He is currently an assistant professor at Kyushu Institute of Technology in JAPAN. He has been working on development of autonomous underwater vehicles (AUVs) and underwater instruments for survey the marine resources. His research interests focus on the automation of marine survey and inspection conducted by humans.

**Kazuo Ishii** received his B.S. and Doctor of Engineering from the University of Tokyo in 1991 and 1996 respectively. His research interests spans Field Robotics, Underwater Robotics, and Neural Networks. He is currently a Professor at the Department of Human Intelligence Systems, Kyushu Institute of Technology.

**Adrian Bodenmann** received the M.Sc. degree in microengineering from the Ecole Polytechnique Federale de Lausanne (EPFL), Lausanne, Switzerland, in 2009. At present he is working at the University of Southampton as a senior research assistant. His research interests are the development of camera systems for high altitude seafloor mapping and algorithms for generating 3D seafloor reconstructions based on photos of the seafloor. He also works on quantifying the certainty in these reconstructions and identifying correlations between identified objects in reconstructions and data from acoustic and chemical sensors.

**Takumi Sato** received the B.S. (2011) in engineering from Tokyo Univ. of Agriculture and Technology, Japan, and the M.S. (2013) in environmentology from Univ. of Tokyo, Japan. He joined National Maritime Research Institute as a researcher in the Offshore Advanced Technology Department in 2016. He has been engaged in the underwater observation system for marine resource consisted of Autonomous Underwater Vehicle.

**Tamaki Ura** (M'91-SM'02-F'07) graduated from the Faculty of Engineering, The University of Tokyo, Japan, in 1972 and received the degree of Doctor of Engineering from the same university in 1977. He retired as Professor emeritus of The University of Tokyo and held positions as the Director and Distinguished Professor of Center for Socio-Robotic Synthesis, Kyushu Institute of Technology, and Director of Underwater Technology Center of National Maritime Research Institute. He has developed various types of Autonomous Underwater Vehicles (AUVs) and related application technologies including navigation methods, a new sensing method using a chemical sensor, precise seafloor mapping methods, a precise seabed positioning system with a resolution of a few centimeters, a new sensing system of the thickness of cobalt-rich crust, etc. Finally, he exemplified using these technologies that AUVs are practicable and valuable tools for deep-sea exploration.

**Akira Asada** (M'05) graduated from the Faculty of Science and Engineering, Waseda University, Tokyo, Japan, in 1977 and received the D.Sc. degree from the University of Tokyo, Tokyo, Japan, in 1995. He retired as the Director of the Center for Integrated Underwater Observation Technology and a Professor at the University of Tokyo, Tokyo, Japan. His research involves the development of acoustic observation systems, including interferrometric and synthetic aperture sonar systems, sub-bottom sonars, and 3-D acoustic imaging systems for marine survey, fishery, and underwater security applications.